

# A Correction Factor to the Two-Bias Method for Determining Mobility-Lifetime Products in Pixelated Detectors

Will Koehler, Michael Streicher, Sean O'Neal, and Zhong He, *Senior Member, IEEE*

**Abstract**—The two-bias method typically used to calculate the mobility-lifetime product ( $\mu\tau$ ) in single-polarity charge sensing detectors, uses induced signals from cathode-side events to measure the  $\mu\tau$ . This method assumes an ideal weighting potential (exactly zero through the bulk and a rapid rise to unity at the anode). When a non-ideal weighting potential (e.g., from a pixelated detector) is used, the  $\mu\tau$  is systematically overestimated. In this work, we characterize this overestimation and present a simple correction factor  $k$  that can be applied to pixelated electrode configurations. It was found that the correction factor is only dependent on the pixel-pitch to detector thickness ratio.

**Index Terms**—Direct measurement of  $\mu_e\tau_e$ , two-bias method, weighting potential correction.

## I. INTRODUCTION

THE mobility-lifetime product ( $\mu\tau$ ) is used to characterize the performance of semiconductor radiation detectors and determine the viability of new materials for gamma-ray spectroscopy and imaging. The traditional method to calculate the electron mobility-lifetime product ( $\mu_e\tau_e$ ) utilizes the Hecht relation:

$$Q = N_0 e_0 \frac{\mu_e \tau_e V}{D^2} \left[ 1 - \exp\left(-\frac{D^2}{\mu_e \tau_e V}\right) \right] \quad (1)$$

where  $Q$  is the induced charge on the cathode or anode,  $N_0$  is the number of electrons generated by the radiation interaction,  $e_0$  is the electron charge,  $V$  is the applied bias, and  $D$  is the detector thickness [1]. Equation (1) assumes a uniform electric field, uniform  $\mu_e\tau_e$ , and that the interactions take place at the cathode surface. During the measurement, alpha-particles or low energy x-rays are used to generate electrons near the cathode surface. The holes are immediately collected and the resulting signal is caused by only the electron drift. The photopeak amplitude (assumed to be proportional to  $Q$ , which is true if ballistic deficit is insignificant) is measured as a function of bias, and the result is fit with (1) to extract  $\mu_e\tau_e$ .

Manuscript received December 8, 2015; revised February 26, 2016; accepted March 22, 2016. Date of publication May 5, 2016; date of current version June 21, 2016. This work was supported by DHS DNDO (SBIR contract #HSHQDC-13-C-00068) through RMD, DOE (Award #DE-AC52-07NA27344) through LLNL, and the National Science Foundation Graduate Research Fellowship.

The authors are with the Department of Nuclear Engineering and Radiological Sciences, University of Michigan, Ann Arbor, MI 48109 USA (e-mail: koehlerw@umich.edu).

Color versions of one or more of the figures in this paper are available online at <http://ieeexplore.ieee.org>.

Digital Object Identifier 10.1109/TNS.2016.2548420

By switching the polarity of the bias,  $\mu_h\tau_h$  can be measured using the same technique.

Mobility-lifetime products based on the Hecht relation have been shown to underestimate the true  $\mu\tau$  due to ballistic deficit and surface trapping [2], [3]. Specifically, the method assumes that surface trapping is minimal and that the shaping time is much longer than the electron drift time. Additionally, curve fitting is required. Work by Jones *et al.* showed that the measured  $\mu_e\tau_e$  can vary by up to 30% when the same data is fit with the Hecht relation by different researchers using different (subjective) fitting constants [3]. Additionally, the authors showed  $\mu_e\tau_e$  variations up to a factor of 5 when they used the Hecht relation and different shaping times, particle types, and particle energy on the same detector.

A more direct measurement of the  $\mu_e\tau_e$  for single polarity charge sensing detectors was developed to overcome many of the issues resulting from the Hecht fitting [2]. Single polarity charge sensing detectors utilize electrode geometry (e.g., coplanar grids [4], pixels [5], Frisch collar devices [6], [7]) to measure the drift of only one type of charge carrier (electron or hole). The technique is particularly useful for materials like CdZnTe (CZT), HgI<sub>2</sub>, and TlBr, where the electron mobility is significantly greater than the hole mobility.

The two-bias method outlined in [2] uses the measurement of cathode-side charge collection efficiency at two different biases to measure the  $\mu_e\tau_e$ :

$$\mu_e\tau_e = \frac{D^2}{\ln\left(\frac{N_1}{N_2}\right)} \left( \frac{1}{V_2} - \frac{1}{V_1} \right) \quad (2)$$

where  $N_1$  and  $N_2$  are the photopeak centroids at biases  $V_1$  and  $V_2$ , respectively. Assuming uniform bulk trapping,

$$N_1(z) = N_0 \exp\left(-\frac{zD}{\mu_e\tau_e V_1}\right) \quad (3)$$

where  $N_0$  is the number of generated electron-hole pairs.

While the two-bias method only requires that  $N_1$  and  $N_2$  be from the same depth, cathode side events are generally chosen because they are the easiest to select, have the lowest uncertainty, and ensure that the measured  $\mu_e\tau_e$  is the average over the entire bulk. Cathode side events are typically selected using the cathode-to-anode signal amplitude ratio (CAR) [5]. Because the depth of interaction can be determined, high energy gamma-rays can be used, reducing the signal-to-noise ratio and improving the results. The two-bias method is not

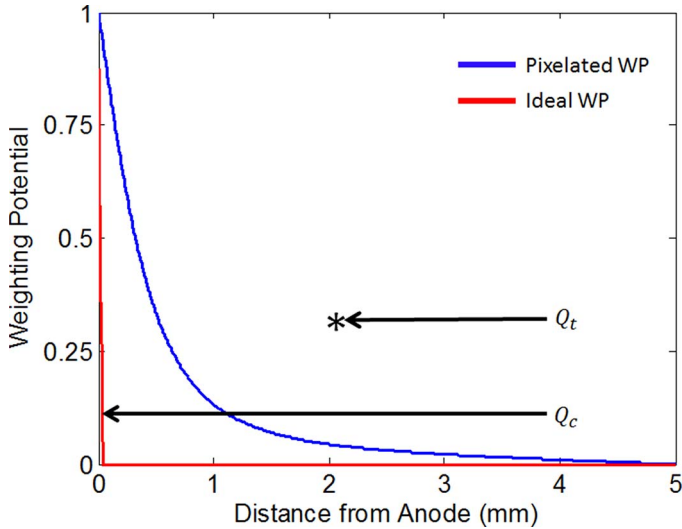


Fig. 1. Weighting potential for an ideal detector and a 5 mm thick pixelated detector with 1 mm pitch. The total charge generated at 4 mm is  $Q_T = Q_t + Q_c$ .

very sensitive to ballistic deficit because the rise time in single-polarity configurations is much shorter than the electron drift time. It is also not sensitive to surface trapping or uncertainty in particle penetration depth because the depth of interaction is accurately determined by the CAR (note that the CAR will ignore any part of the bulk with heavy surface trapping). Additionally, due to the ratio of the  $N_1$  and  $N_2$  signals, the two-bias method is not sensitive to many systematic effects like non-uniform charge collection and depth-dependent performance variation. Specific descriptions of these improvements are detailed in [2].

The standard two-bias method assumes a uniform electric field; however, unlike with Hecht fitting, these electric field non-uniformity effects can be corrected (see Section V). It should be noted that the two-bias method assumes that the electron drift speed is only determined by the applied bias and the mobility (ignoring diffusion and inter-cloud repulsion). This condition is achievable with realistic electric field strengths ( $> 1000$  V/cm).

Due to very good position and energy resolution, pixelated electrodes are popular for 3D position sensitive semiconductor detectors [5]–[12]. Because of the simplicity and accuracy of the two-bias method, many researchers have used it to characterize  $\mu_e\tau_e$  in pixelated detectors [8], [11]–[14]. However, the original two-bias method assumes an ideal weighting potential for single-polarity charge sensing; specifically, zero throughout the bulk and a rapid increase to one at the anode surface (see Fig. 1, red curve). In this work, we show that using the two-bias method on pixelated detectors systematically overestimates the  $\mu_e\tau_e$  by up to 20% for common detector thicknesses and electrode geometries. As a result, a simple correction factor is required:

$$\mu_e\tau_e = k(\mu_e\tau_e)_{TwoBias} \quad (4)$$

where  $(\mu_e\tau_e)_{TwoBias}$  is the electron mobility-lifetime product calculated from (2) using a pixelated detector. The correction

factor  $k$  depends on the interaction depth used to calculate  $(\mu_e\tau_e)_{TwoBias}$ . While any depth could be used, this work focuses on the cathode-side  $k$  because cathode-side events are most commonly used to calculate  $\mu_e\tau_e$ . The origin of  $k$  and values for typical electrode geometries are explored in this work.

## II. ORIGIN OF THE CORRECTION FACTOR

The Shockley-Ramo theorem states that the induced charge on an electrode is equal to the generated charge multiplied by the weighting potential change [15], [16]. (See [17] for a full discussion of the Shockley-Ramo theorem and its implications to pixelated and coplanar grid electrodes). The two-bias method assumes that any trapped charge does not contribute to the signal because it does not go through any weighting potential change (the ideal weighting potential is exactly zero through the bulk).

Consider the case outlined in Fig. 1 where an interaction occurs at depth  $z = 4$  mm. (Note:  $z = 4$  mm is an arbitrary depth and was chosen because it highlights the different effects of the trapped vs. untrapped charge. While typical  $\mu_e\tau_e$  calculations are done at the cathode surface ( $z = 5$  mm), the electron clouds from those events must pass through  $z = 4$  mm.) To simplify the scenario, let  $Q_t$  be all the trapped charge and let it drift 2 mm before being trapped. If  $Q_c$  is the collected (untrapped) charge, then the total generated charge is  $Q_T = Q_t + Q_c$ .

If  $N'_1$  is the signal from a pixelated weighting potential and  $N_1$  is the signal from an ideal weighting potential (which is assumed in (2)), then  $N'_1$  has an added component compared to  $N_1$  because the trapped charge  $Q_t$  goes through a weighting potential change (and therefore contributes to the signal) in the pixelated case but not in the ideal case.  $N'_1$  also has a subtracted component because the collected charge  $Q_c$  in the pixelated case does not go through the full weighting potential. The relationship between  $N_1$  and  $N'_1$  in the example outlined in Fig. 1 is:

$$N'_1 = N_1 [1 - \phi(4)] + (N_0 - N_1) \langle \Delta\phi(4, 2) \rangle \quad (5)$$

where  $\phi(4)$  is the pixelated weighting potential at  $z = 4$  mm, and  $\langle \Delta\phi(4, 2) \rangle$  is the average change in pixelated weighting potential between  $z = 4$  mm and  $z = 2$  mm. The first term represents the subtracted signal as a result of  $Q_c$  not going through the full weighting potential. The second term represents the added signal from  $Q_t$  which goes through a non-zero weighting potential change. Note that if cathode side events are chosen, the first term goes to  $N_1$ .

In the real case, a small amount of charge  $\delta q_t$  is trapped when the untrapped generated charge goes through an incremental depth,  $\delta z$ . If the charge drift is divided into a number of depth bins, then (5) can be replaced with a finite sum:

$$N'_1(z_j) = N_1(z_j) [1 - \phi(z_j)] + \sum_{i=1}^j [N_1(z_{i-1}) - N_1(z_i)] \left[ \frac{\phi(z_i) - \phi(z_{i-1})}{2} \right] \quad (6)$$

where  $z_j$  is the distance of the  $j^{\text{th}}$  bin from the anode. Again, the first and second terms account for the trapped and

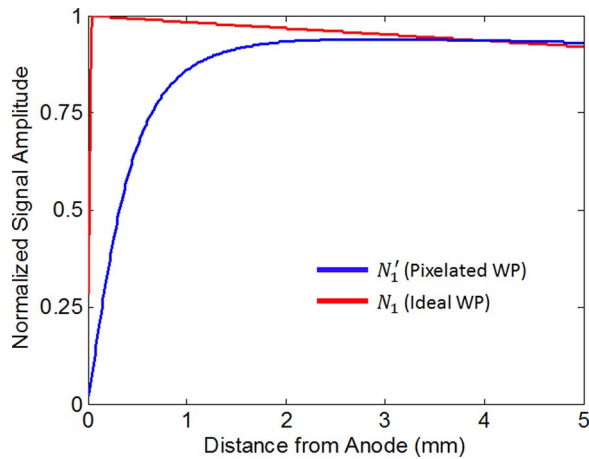


Fig. 2. Normalized signal amplitudes as a function of depth for pixelated and ideal weighting potentials.

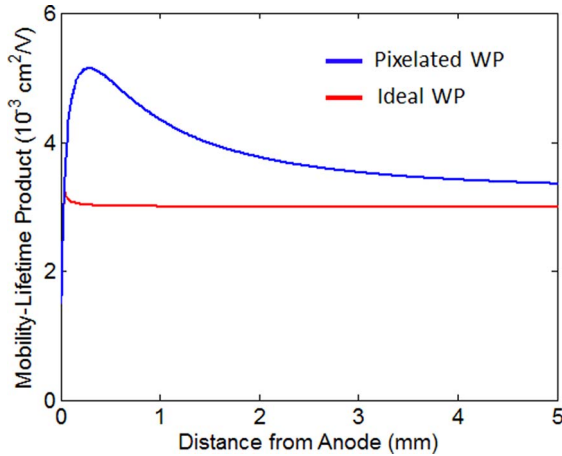


Fig. 3. Calculated  $\mu_e\tau_e$  for an ideal detector and for a 5 mm thick pixelated detector with 1 mm pitch. The  $\mu_e\tau_e$  was set to  $3 \times 10^{-3} \text{ cm}^2/\text{V}$ .

untrapped charge, respectively.  $N_1(z_i)$  is calculated using (3) so  $N_1(z_{i-1}) - N_1(z_i) = \delta q_i$ .

### III. SIMULATION RESULTS

Fig. 2 shows  $N_1$  and  $N'_1$  calculated using (3) and (6), respectively, for the ideal and pixelated weighting potentials shown in Fig. 1. One-thousand depth bins were used for the calculations. This was chosen to ensure that the average weighting potential change multiplied by the trapped signal approximated the signal induced by the trapped charge. The number of bins was increased until a consistent solution was achieved. The signals are normalized because  $N_0$  was set to one. The detector bias  $V_1$  was 1000 V and the  $\mu_e\tau_e$  was set to  $3 \times 10^{-3} \text{ cm}^2/\text{V}$ , typical values for 5 mm thick semiconductor detectors. Near the cathode surface, the second term in (6) dominates and  $N'_1 > N_1$ . Through the rest of the bulk, the first term dominates and  $N'_1 < N_1$ . The same method was used to generate  $N_2$  and  $N'_2$  at  $V_2 = 1500 \text{ V}$ .

Fig. 3 shows the calculated  $\mu_e\tau_e$  using (2) for the pixelated and ideal weighting potentials shown in Fig. 1. The  $N_1$  and  $N_2$  signals calculated above (e.g.,  $N_1$  shown in Fig. 2) were used

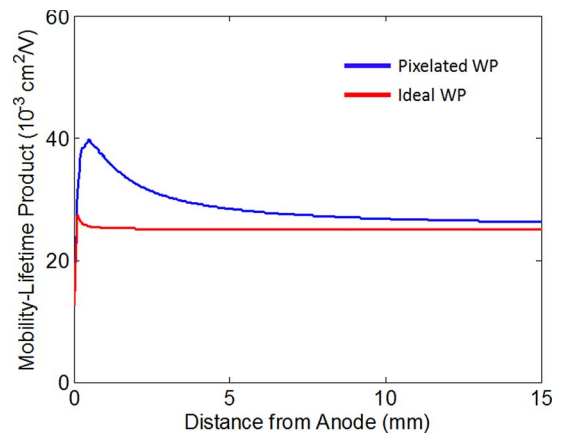


Fig. 4. Calculated  $\mu_e\tau_e$  for an ideal detector and for a 15 mm thick pixelated detector with 1.72 mm pitch. The  $\mu_e\tau_e$  was set to  $25 \times 10^{-3} \text{ cm}^2/\text{V}$ .

for the ideal case and the  $N'_1$  and  $N'_2$  signals were used for the pixelated case. The  $N_1$ ,  $N_2$ ,  $N'_1$ , and  $N'_2$  signals were calculated using  $\mu_e\tau_e = 3 \times 10^{-3} \text{ cm}^2/\text{V}$ ; therefore, the expected  $\mu_e\tau_e$  at all depths was  $3 \times 10^{-3} \text{ cm}^2/\text{V}$ . Using the ideal weighting potential, the calculated  $\mu_e\tau_e$  (red curve in Fig. 3) equals the expected  $\mu_e\tau_e$  at all depths except right at the anode where there is a rapid change in weighting potential (note that the rise in calculated  $\mu_e\tau_e$  near the anode is the result of binning; at some point, the weighting potential had to increase to one). For the pixelated detector, the calculated  $\mu_e\tau_e$  (blue curve in Fig. 3) is consistently overestimated compared to the expected  $\mu_e\tau_e$ . At the cathode surface (where most published work using (2) calculate  $N_1$  and  $N_2$ ), the  $\mu_e\tau_e$  is overestimated by  $\sim 10\%$ . Therefore, a correction factor of  $k = 0.896$  needs to be applied to  $\mu_e\tau_e$  calculations utilizing the two-bias method when cathode side events are used with 5 mm thick pixelated detectors with 1 mm pixel pitch.

Fig. 4 shows the calculated  $\mu_e\tau_e$  for a 15 mm thick detector with 1.72 mm pitch. The  $\mu_e\tau_e$  was set to  $25 \times 10^{-3} \text{ cm}^2/\text{V}$  and the biases were  $V_1 = 2500 \text{ V}$  and  $V_2 = 3000 \text{ V}$ . The selected electrode configuration,  $\mu_e\tau_e$ , and biases in Fig. 4 matched the experimental parameters discussed in Sec. IV. While the profile in Fig. 4 is similar to Fig. 3, the magnitude of the overestimation decreased because the weighting potential of a 15 mm thick detector with 1.72 mm pixel pitch is closer to the ideal weighting potential. The correction factor for this geometry is  $k = 0.941$ .

Table I shows the cathode-side correction factor for common single-polarity charge sensing electrode configurations with 100  $\mu\text{m}$  gap between pixels. The uncertainties were estimated as the standard deviation of the correction factor for different pixel locations (i.e., center pixel, edge pixel, between center and edge pixel). The uncertainty for all cases was less than 0.33% which is significantly lower than typical uncertainties reported for  $\mu_e\tau_e$  values ( $\sim 5 - 10\%$ ). The correction factor does not depend on the  $\mu_e\tau_e$  or the bias values  $V_1$  and  $V_2$  because the origin of the problem is the shape of the weighting potential. This was confirmed by changing  $V_1$ ,  $V_2$ , and  $\mu_e\tau_e$ ; no change was observed in the resulting profile. (Note that when  $\mu_e\tau_e$  was changed, the relative scale

TABLE I  
CORRECTION FACTORS FOR COMMON SINGLE-POLARITY CHARGE SENSING CONFIGURATIONS WITH 100  $\mu\text{m}$  GAP BETWEEN PIXELS. THE ERRORS ON THE CORRECTION FACTORS ARE LESS THAN 0.003.

Dimensions (mm <sup>3</sup> )	Pixel Pitch (mm)	Pitch/Thickness	Correction Factor
5x5x5	1	0.2	0.896
5x5x5	2	0.4	0.796
10x10x5	2	0.4	0.812
10x10x10	1	0.1	0.949
10x10x10	2	0.2	0.896
20x20x10	1	0.15	0.924
20x20x10	1.5	0.25	0.876
20x20x10	2.5	0.1	0.950
20x20x15	1	0.067	0.967
20x20x15	1.72	0.115	0.941
20x20x15	2	0.133	0.932
40x40x5	1.25	0.25	0.877
40x40x5	1.4	0.28	0.863
40x40x5	1.75	0.35	0.833
40x40x5	2	0.4	0.813

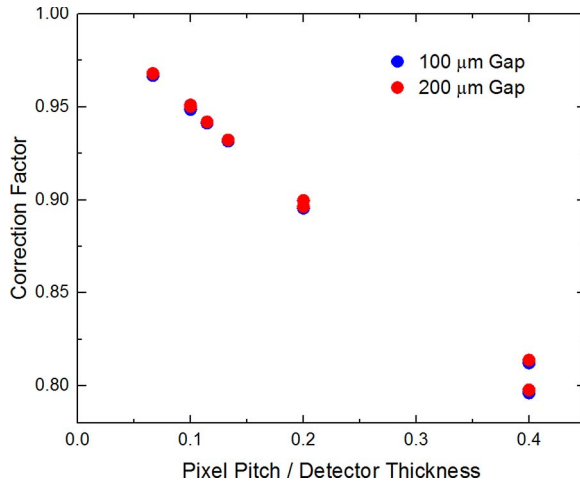


Fig. 5. Correction factor for various pitch/thickness ratios using 100  $\mu\text{m}$  (blue) and 200  $\mu\text{m}$  (red) gaps.

of the calculated  $\mu_e\tau_e$  also changed; however, the fractional profile, and therefore the correction factor, was unaffected.)

Fig. 5 shows the correction factor for different pixel pitch to detector thickness ratios (PDR) when a 100  $\mu\text{m}$  (blue) and 200  $\mu\text{m}$  (red) gap between pixels was used. In order to maintain the correct pitch, the pixel pad was decreased by 100  $\mu\text{m}$  for the 200  $\mu\text{m}$  cases. The change to the correction factor was less than 0.003 for all configurations. Therefore, the size of the gap does not significantly affect the correction factor.

Fig. 6 shows the correction factor as a function of the PDR. The correction factor is linear as a function of PDR except for the  $5 \times 5 \times 5 \text{ mm}^3$  detector with 2 mm pixel pitch. For this case, the pixel is large compared to the detector face, and the correction factor decreases. When the detector face was increased to  $40 \times 40 \text{ mm}^2$ , the correction factor was consistent with the other data. The least squares line of best fit for all electrode configurations except the  $5 \times 5 \times 5 \text{ mm}^3$  detector with 2 mm pitch was:

$$k = -0.459 * PDR + 0.993. \quad (7)$$

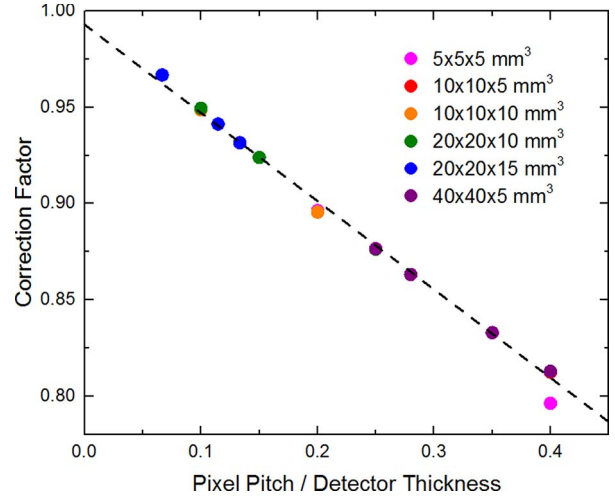


Fig. 6. Correction factor for various pitch/thickness ratios for 100  $\mu\text{m}$  gaps. The uncertainties were all less than 0.003.

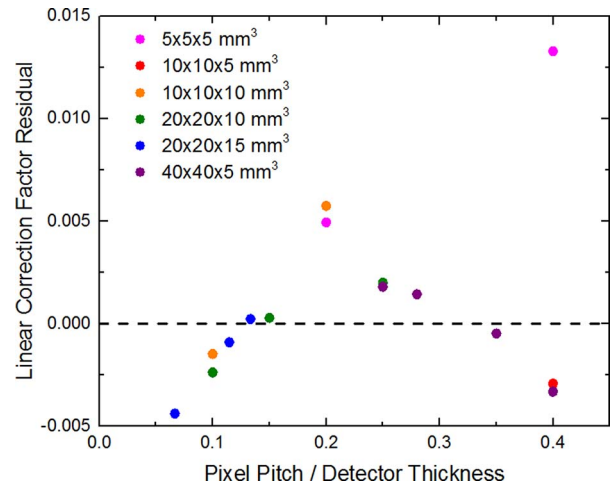


Fig. 7. Correction factor residuals from the linear least-squares line of best fit.

The errors on the slope and intercept were 0.007 and 0.002, respectively. Equation (7) provides a simple method to calculate the cathode-side correction factor for the two-bias method. Equation (7) is limited to detector sizes modeled in this work (listed in Table I), specifically, detectors equal to or larger than  $5 \times 5 \times 5 \text{ mm}^3$  with 1 mm pitch, equal to or smaller than  $20 \times 20 \times 15 \text{ mm}^3$  with 2 mm pitch or  $40 \times 40 \times 5 \text{ mm}^3$  with 2 mm pitch, and with a PDR between 0.07 and 0.4. This range encompasses typical geometries that have utilized the two-bias method. Most of the contribution to the correction factor results from the rapid weighting potential change near the anode. The extent of the rapid change region is roughly equal to the detector pixel pitch. Therefore, the fraction of the detector which has a non-ideal weighting potential changes linearly with PDR. As a result, (7) is also linear with PDR.

Fig. 7 shows the residual between the best-fit line and the correction factors. All the residuals except the  $5 \times 5 \times 5 \text{ mm}^3$  detector with 2 mm pitch are within 0.9% of the best-fit line. There is a parabolic trend between the true value of the correction factor and the linear fit based on the PDR.

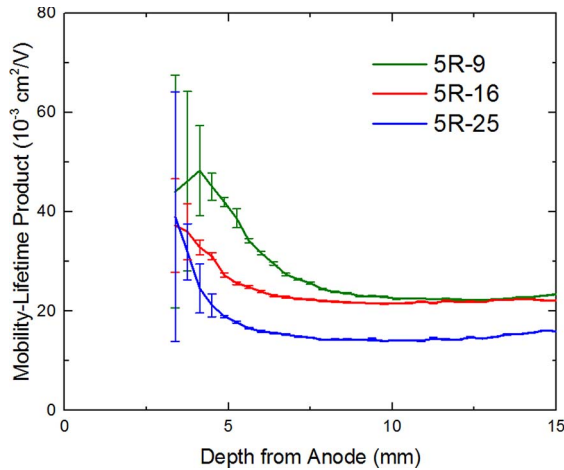


Fig. 8. Depth dependent  $\mu_e\tau_e$  calculated from (2) in a 15 mm thick CZT detector with 1.72 mm pixel pitch.

In practice, this offset is much smaller compared to the uncertainty inherent in the  $\mu_e\tau_e$  measurement. For high performing detectors ( $< 1\%$  FWHM at 662 keV), most of the uncertainty comes from uncertainty in the interaction depth [2]. Large pixelated CZT detectors have a depth uncertainty of about 2.5% (40 depth bins across 15 mm). By propagating the 0.9% maximum error in  $k$  through (4), the  $\mu_e\tau_e$  uncertainty increases to 2.7% (compared to 2.5%), a marginal increase on the lowest uncertainty case. If the error increase is unacceptable, the true correction factor can be calculated by modeling the weighting potential using the exact dimensions of the device.

#### IV. EXPERIMENTAL DATA WITH 15 mm THICK CZT DETECTORS

Previous work has shown that the CAR accurately determines the depth of interaction for 662 keV gamma rays in 15 mm thick pixelated CZT detectors [18]. The CAR parameter was used to break up the 662 keV energy spectrum of three detectors into 40 depth bins. Equation (2) was evaluated as a function of depth using the depth-dependent photopeak centroids as  $N'_1$  and  $N'_2$ . The  $\mu_e\tau_e$  profiles calculated for the three detectors is shown in Fig. 8. Note that the real  $\mu_e\tau_e$  profile is likely much more uniform across the bulk; the apparent non-uniformity is a result of using the two-bias method on a pixelated detector. The profiles are not shown for depths under 3.5 mm because of high uncertainty, a result of the fast anode-side weighting potential change.

While the general shape of Fig. 8 matches Fig. 4 (the  $\mu_e\tau_e$  profile is fairly uniform through most of the bulk and rises quickly near the anode) the coefficient of determination between the  $\mu_e\tau_e$  values for detector 5R-9 (green curve in Fig. 8, shown again in green curve in Fig. 9) and the simulated values (blue curve in Fig. 9) is only  $R^2 = 0.17$ . Additionally, the specific depth where the profile changes from uniform to sharply rising varies from detector to detector.

It is well known that the internal electric field profile for semiconductor detectors is non-uniform, especially for thicker detectors [10], [19]. Instead, the electric field is weaker

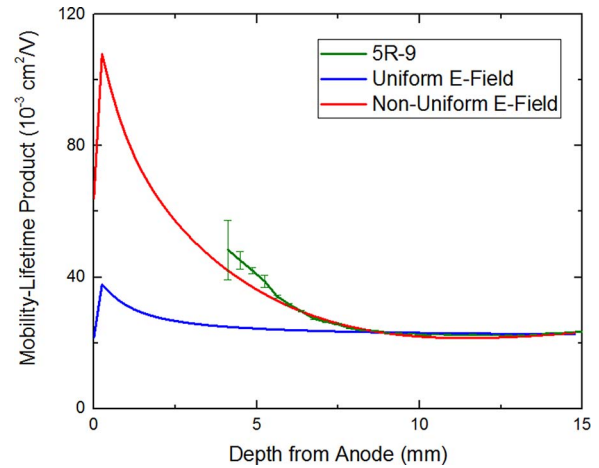


Fig. 9. Effect of a non-uniform electric field on the  $\mu_e\tau_e$  profile.

near the center of the device and stronger near both the cathode and anode. Fig. 9 shows the expected  $\mu_e\tau_e$  profile for a 15 mm thick detector with 1.72 mm pitch with expected  $\mu_e\tau_e = 28 \times 10^{-3} \text{ cm}^2/\text{V}$ . The profile is shown for both a uniform electric field and one that is weaker in the center (an approximation of the expected electric field in detector 5R-9). The cathode-side calculation of the  $\mu_e\tau_e$  is largely unaffected by the non-uniform electric field, but the transition depth between uniform  $\mu_e\tau_e$  and sharply rising  $\mu_e\tau_e$  changes. Additionally, there is a slight dip near the cathode side before the non-uniform profile increases toward the anode side. When the electric field effects are corrected, the coefficient of determination between the experimental  $\mu_e\tau_e$  (green curve in Fig. 9) and the simulated  $\mu_e\tau_e$  values (red curve in Fig. 9) increases to  $R^2 = 0.90$ , indicating much better agreement.

#### V. COMPARISON TO OTHER EFFECTS

[3] outlines other effects which can change the calculation of  $\mu_e\tau_e$ , including shaping time, particle type, and particle energy. As mentioned in Section I, the two-bias method, unlike the Hecht fitting method, is insensitive to ballistic deficit as long as the shaping time is much longer than the anode collection time (typically much shorter than the full drift time for single-polarity charge sensing configurations). Similarly, the two-bias method is insensitive to surface trapping and will not show a significant difference for particle type and energy (note: using low energy particles could increase the signal to noise ratio and increase the precision of  $\mu_e\tau_e$ , but not the accuracy).

Both Hecht fitting and the two-bias method are sensitive to non-uniform electric fields. If a high resolution profile of the electric field is known, it can be used to correct the  $\mu_e\tau_e$  profile using the more complete form of (2):

$$\mu_e\tau_e = \frac{1}{\ln\left(\frac{N_1}{N_2}\right)} \left[ \int_0^z \frac{1}{E_2(z')} dz' - \int_0^z \frac{1}{E_1(z')} dz' \right] \quad (8)$$

where  $E_1$  and  $E_2$  are the electric field profiles at different biases. Note that for a constant electric field, (8) reduces to (2).

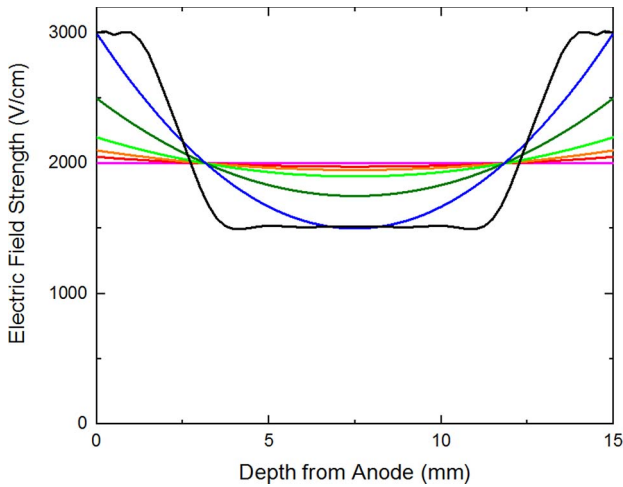


Fig. 10. Continuous function, non-uniform electric field profiles with similar characteristics of profiles obtained from cathode signal analysis.

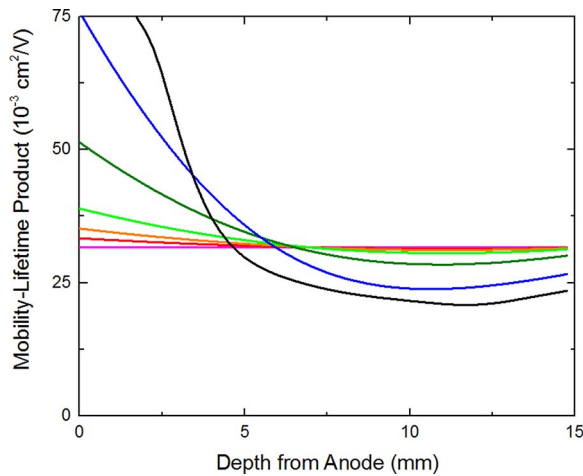


Fig. 11. Mobility-lifetime profiles for non-uniform electric fields shown in Fig. 10 (the colors are consistent between figures). Weighting potential effects were controlled by using an ideal weighting potential.

While there is currently no technique to measure the electric field profile in thick semiconductor detectors with the fidelity required to use (8), the profile can be approximated with continuous functions comparable to profiles obtained from cathode waveform analysis [10]. These electric field profiles can be used to estimate the magnitude of the non-uniform electric field effect on the  $\mu_e\tau_e$  measurement.

Fig. 10 shows continuous functions of non-uniform electric field profiles. Using these profiles and (8), the resulting  $\mu_e\tau_e$  profiles were calculated and are shown in Fig. 11. The colors are consistent between the two figures. The magnitude of the non-uniform electric field effect to the two-bias method was estimated by calculating the change to the  $\mu_e\tau_e$  value at the cathode side. This was estimated to be 30% for the most extreme electric field profile (black curve) and 5% for a moderate profile (dark green curve). It should be noted that thin detectors (5 mm thick) tend to have a much more uniform electric field compared to thick (15 mm thick) detectors, in which case the weighting potential correction dominates.

In either case, if the electric fields effects are corrected, the weighting potential correction factor must be applied.

## VI. CONCLUSIONS

The two-bias method provides a simple way to calculate the  $\mu_e\tau_e$  for single-polarity charge sensing devices. However, the electrode geometry must be taken into account or the calculated  $\mu_e\tau_e$  will be systematically overestimated. This work provides a simple correction factor for the two-bias method when non-ideal weighting potentials and cathode-side centroids are used. The expected depth-dependent  $\mu_e\tau_e$  profile was compared to experimental results obtained from a 15 mm thick CZT detector with 1.72 mm pixel pitch. The correlation between experimental and simulated results was  $R^2 = 0.9$  when electric field effects were corrected.

Some of the correction factors for detectors with small PDR are less than typical uncertainties reported for  $\mu_e\tau_e$ . However, this paper addresses a systematic uncertainty not accounted for during random uncertainty propagation. Therefore, some correction factor should be applied to all  $\mu_e\tau_e$  values calculated using the two-bias method when detectors with non-ideal weighting potentials are used. This includes all other single-polarity charge sensing configurations like coplanar grid and Frisch-collar grid detectors. The magnitude of the correction factor will depend on how well the weighting potential matches the ideal weighting potential. This work provides this correction factor for pixelated detectors with common sizes and pixel pitches and a method to calculate the correction factor for any weighting potential.

## REFERENCES

- [1] T. Schlesinger and R. James, *Semiconductors for Room Temperature Nuclear Detection Applications*, ser. Semiconductors and Semimetals. New York, NY, USA: Academic, 1995.
- [2] Z. He, G. F. Knoll, and D. K. Wehe, "Direct measurement of product of the electron mobility and mean free drift time of CdZnTe semiconductors using position sensitive single polarity charge sensing detectors," *J. App. Phys.*, vol. 84, no. 10, 1998.
- [3] K. A. Jones, A. Datta, K. G. Lynn, and L. A. Franks, "Variations in  $\mu\tau$  measurements in cadmium zinc telluride," *J. App. Phys.*, vol. 107, 2010.
- [4] P. N. Luke, "Single-polarity charge sensing in ionization detectors using coplanar electrodes," *Appl. Phys. Lett.*, vol. 65, 1994.
- [5] Z. He, W. Li, and G. Knoll, "3-D position sensitive CdZnTe gamma-ray spectrometers," *Nucl. Instrum. Methods Phys. Res. A*, vol. 422, pp. 173–175, 1999.
- [6] A. Kargar, A. Jones, W. McNeil, M. Harrison, and D. McGregor, "CdZnTe Frisch collar detectors for  $\gamma$ -ray spectroscopy," *Nucl. Instrum. Methods Phys. Res. A*, vol. 558, pp. 497–503, 2006.
- [7] A. E. Bolotnikov, G. C. Camarda, G. A. Carini, M. Fiederle, L. Li, D. S. McGregor, W. McNeil, G. W. Wright, and R. B. James, "Performance characteristics of Frisch-grid CdZnTe detectors," *IEEE Trans. Nucl. Sci.*, vol. 53, no. 2, pp. 607–614, 2006.
- [8] F. Zhang, C. Herman, Z. He, D. DeGeronimo, E. Vernon, and J. Fried, "Characterization of the H3D ASIC readout system and  $6.0^3$  3-D position sensitive CdZnTe detectors," *IEEE Trans. Nucl. Sci.*, vol. 59, no. 1, pp. 236–242, Feb. 2012.
- [9] Y. Zhu, S. E. Anderson, and Z. He, "Sub-pixel sensing for pixelated, 3-D position sensitive, wide band-gap, semiconductor gamma-ray detectors," *IEEE Trans. Nucl. Sci.*, vol. 58, no. 3, pp. 1400–1409, Jun. 2011.
- [10] W. Koehler, Z. He, S. O'Neal, H. Yang, H. Kim, L. Cirignano, and K. Shah, "Quantification of the conditioning phase in cooled pixelated TlBr detectors," *IEEE Trans. Nucl. Sci.*, vol. 62, no. 4, pp. 1785–1790, 2015.
- [11] K. Hitomi, T. Onodera, T. Shoji, Y. Hiratate, and Z. He, "TlBr gamma-ray spectrometers using the depth sensitive single polarity charge sensing technique," *IEEE Trans. Nucl. Sci.*, vol. 55, no. 3, pp. 1781–1784, Jun. 2008.

- [12] J. E. Bacia and Z. He, "Spectroscopy on thick HgI<sub>2</sub> detectors: A comparison between planar and pixelated electrodes," *IEEE Trans. Nucl. Sci.*, vol. 50, no. 4, pp. 1220–1224, Aug. 2003.
- [13] L. J. Meng, Z. He, B. Alexander, and J. Sanodval, "Spectroscopic performance of thick HgI<sub>2</sub> detectors," *IEEE Trans. Nucl. Sci.*, vol. 53, no. 3, pp. 1706–1212, Jun. 2006.
- [14] I. Jung, H. Krawczynski, A. Burger, M. Guo, and M. Groza, "Detailed studies of pixelated CZT detectors grown with the modified horizontal Bridgman method," *Astropart. Phys.*, vol. 28, pp. 397–408, 2007.
- [15] W. Shockley, "Currents to conductors induced by a moving point charge," *J. App. Phys.*, pp. 635–636, 1938.
- [16] S. Ramo, "Currents induced by electron motion," *Proc. I.R.E.*, p. 584, Sep. 1939.
- [17] Z. He, "Review of the Shockley-Ramo theorem and its application in semiconductor gamma-ray detectors," *Nucl. Instrum. Methods Phys. Res. A*, vol. 463, pp. 250–267, 2001.
- [18] W. Kaye, *Energy and Position Reconstruction in Pixelated CdZnTe Detectors*, Ph.D. dissertation dissertation, Univ.f Michigan, Ann Arbor, MI, USA, 2012.
- [19] Y. Boucher, F. Zhang, W. Kaye, and Z. He, "New measurement technique for the product of the electron mobility and mean free drift time for pixelated semiconductor detectors," *Nucl. Instrum. Methods Phys. Res. A*, vol. 671, pp. 1–5, 2012.